Scanning Microscopy

Volume 1994
Number 8 *The Science of Biological Microanalysis*

Article 20

2-7-1994

Biological Electron Energy Loss Spectroscopy in the Field-Emission Scanning Transmission Electron Microscope

R. D. Leapman
NCRR, leapman@helix.nih.gov

S. Q. Sun
NCRR

J. A. Hunt
Gatan R & D

S. B. Andrews
NINDS

Scanning Microscopy Supplement 8, 1994 (pages 245-259) 0892-953X/94$5.00+.25
Scanning Microscopy International, Chicago (AMF O'Hare), IL 60666 USA

BIOLOGICAL ELECTRON ENERGY LOSS SPECTROSCOPY IN THE FIELD-EMISSION SCANNING TRANSMISSION ELECTRON MICROSCOPE

R.D. Leapman[1*], S.Q. Sun[1], J.A. Hunt[2] and S.B. Andrews[3]

[1]Biomedical Engineering & Instrumentation Program, NCRR, National Institutes of Health, Bethesda, MD 20892
[2]Gatan R & D, Pleasanton, CA 94566
[3]Laboratory of Neurobiology, NINDS, National Institutes of Health, Bethesda, MD 20892, USA.

(Received for publication December 2, 1993, and in revised form February 7, 1994)

Abstract

The dedicated scanning transmission electron microscope (STEM) combined with parallel electron energy loss spectroscopy (EELS) provides a very sensitive means of detecting specific elements in small structures. EELS is more sensitive than optimized energy-dispersive X-ray spectroscopy by a factor of about three for calcium. Measurement of such low concentrations requires special processing methods such as difference-acquisition techniques and multiple least squares procedures for fitting reference spectra. By analyzing data recorded at each pixel in a spectrum-image it is possible to map quantitatively the elemental distributions in a specimen. It is possible to prepare cryosections that are sufficiently thin to avoid excessive plural inelastic scattering so analysis can be performed at 100 keV beam energy. Under optimal conditions, a resolution of 10 nm and detection limits of a few atoms are achievable for elements such as calcium, phosphorus and iron. In the field emission STEM certain types of chemical information can be extracted from biological specimens. Valence EELS has been exploited to measure water distributions in frozen hydrated cryosections.

Key Words: Electron energy loss spectroscopy (EELS), parallel-detection, scanning transmission electron microscopy (STEM), cryosections, calcium, detection limits, water content, elemental mapping, difference-spectra, radiation damage.

*Address for Correspondence:
Richard D. Leapman
Biomedical Engineering & Instrumentation Program
Bldg. 13, Rm. 3W13, National Institutes of Health
Bethesda, MD 20892, USA
Telephone Number: (301) 496-2599
Fax Number: (301) 496-6608
E-mail: leapman@helix.nih.gov

Introduction

As a result of several improvements over recent years electron energy loss spectroscopy (EELS) has gradually emerged as a useful technique for analyzing biological specimens in the scanning transmission electron microscope (STEM). These advances have been mainly facilitated by the development of parallel-detection spectrometers that can be coupled to microscopes with high-brightness sources, as well as the availability of new techniques for processing the spectra (Shuman, 1981; Shuman and Kruit, 1985; Krivanek *et al.*, 1987; Krivanek *et al.*, 1989). For example, it has been demonstrated that EELS offers extremely high sensitivity for analysis of the biologically important element calcium in cryosectioned tissue and that it is possible to achieve detection limits that are lower than for energy-dispersive X-ray spectroscopy (EDXS) (Shuman and Somlyo, 1987; Leapman *et al.*, 1993). Such results are not only achievable in point analyses but elemental distributions can be obtained by sophisticated spectrum-imaging methods. The high spatial resolution of the STEM has in fact provided an unprecedented microanalytical capability permitting EELS analysis of isolated macromolecules with a detectability of a few atoms (Isaacson and Johnson, 1975; Leapman and Andrews, 1992). The richness of the inelastic scattering spectrum and the narrow energy spread of the field-emission source also provide the possibility of extracting more detailed chemical information about the distributions of specific compounds inside subcellular compartments (Sun *et al.*, 1993). As for the other microanalytical techniques, rapid freezing and cryosectioning are usually required for EELS analysis to preserve the elemental composition of biological systems on the microscopic scale (Zierold, 1988). For example, it is well known that conventional fixation and embedding methods redistribute ions and small molecules. Previously, this requirement has been a problem for EELS analysis because of the difficulty in preparing cryosections that are thin enough to avoid severe plural inelastic scattering (Leapman and Ornberg,

1988). Fortunately, the developments in EELS have been accompanied by advances in cryopreparation techniques, so that it is now possible to cut cryosections suitably thin for analysis (Michel *et al.*, 1992; Buchanan *et al.*, 1993). The aims of this paper are to demonstrate the current capabilities of EELS in the context of the dedicated STEM and to suggest some future directions for research.

Instrumental Considerations

The STEM has a number of important features that are useful for performing EELS analysis on biological specimens. Most importantly, it has a high-brightness field-emission source and this type of instrument is therefore capable of providing a sub-nanometer diameter electron probe (Crewe, 1970). Another important feature of the STEM is that elastically scattered electrons can be collected with extremely high efficiency by means of an annular dark-field detector situated after the specimen. The main biological applications of STEM have involved this image mode whereby the masses of large macromolecular assemblies can be accurately determined (Wall, 1979; Wall and Hainfeld, 1986; Engel, 1978). In such experiments data must be recorded at low dose ($< 10^3$ e/nm^2) and the probe current is typically reduced to the picoampere range. Apart from its use as a structural device, the STEM also offers exciting potential as a microanalytical tool. It was nearly twenty years ago that Isaacson and Johnson (1975) predicted that near-single atom sensitivity should be achievable by combining EELS with the field-emission STEM. Even without an optimized system these authors were able to demonstrate detection of fewer that 4000 iron atoms in a single ferritin molecule. In fact, the field-emission STEM is an ideal microanalytical instrument because it is capable of providing very large currents (about 10 nanoamperes) into probe diameters of around 5 nm. These conditions are optimal for microanalysis of subcellular structures by EELS, but it is only recently that this possibility has been fully realized because of two other requirements. First, the handling of cryosectioned tissue requires a stable cryotransfer specimen stage which has only recently become available (Andrews and Leapman, 1989; Nichols and Bovey, 1989). Second, it is essential to collect the energy loss spectrum in parallel so that detection limits can be optimized (Shuman and Somlyo, 1987).

Figure 1 shows a simplified schematic diagram of the system used in the present work, a VG Microscopes HB501 STEM. This instrument maintains an ultra-high vacuum (approximately 3×10^{-9} Pa at the gun and approximately 3×10^{-7} Pa at the specimen chamber). It is

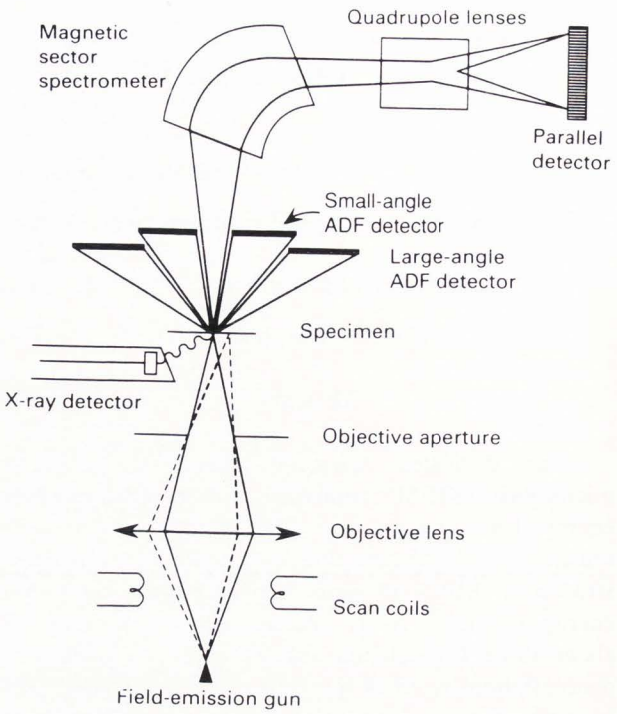

Figure 1: Schematic diagram of VG Microscopes STEM: field-emission source and condenser and objective lenses provide focused probe of 100 keV electrons that is digitally scanned across specimen. Samples are cryotransferred into microscope at liquid nitrogen temperature and are freeze-dried under controlled conditions. Elastically scattered electrons are collected by annular dark-field (ADF) detectors that provide morphological information. Electrons passing through ADF aperture are dispersed by magnetic sector spectrometer; quadruple lenses magnify dispersion and spectrum is collected in parallel by photodiode array detector coupled to single crystal YAG scintillator.

typically operated at a beam energy of 100 keV and is equipped with a cryotransfer specimen stage as well as a Gatan model 666 electron energy loss spectrometer (Krivanek *et al.*, 1987; Krivanek *et al.*, 1989). Electrons pass through the central aperture of an annular dark-field (ADF) detector and then into the magnetic field of the 90° sector after which the energy dispersion is magnified by a series of quadruple lenses. The aperture of the ADF detector defines the spectrometer acceptance angle. An electrostatically isolated drift tube running through the spectrometer can be used to apply precise energy offsets to the spectrum. This feature is utilized for energy calibration and for acquiring difference-spectra. The energy loss spectrum is recorded in parallel by means of a 1024-channel photodiode array detector coupled to a yttrium aluminum garnet (YAG) scintillator

by a fiber-optic plate. The ADF detector provides a morphological elastic image of the specimen simultaneously with the inelastic EELS data. An ultrathin window EDXS detector (Noran Micro-ZHV) is also available to provide complementary information about concentrations of elements that are not suitable for EELS analysis (e.g., sodium and potassium).

The photodiode array is read out in 25 ms, and the integration time can be varied from 25 ms for high spectral intensities to several seconds for weak intensities so that the effective dynamic range of the array is $>10^6$. In order to minimize the detector dark-current the temperature of the photodiode array is reduced by means of a thermoelectric cooler. The attainable energy resolution of the spectrometer is approximately 0.4 eV as determined by the intrinsic energy width of the field-emission source. The probe current could be measured both by deflecting the beam onto a shield surrounding the photodiode array and also by integrating the number of direct photodiode counts in the zero-loss peak. The conversion factor relating the two measurements was approximately 40 incident electrons per photodiode count. Spectra were acquired using the Gatan EL/P program running on an Apple Macintosh II computer (Kundmann *et al.*, 1990).

Another computer system was used to acquire EELS images as described previously (Hunt and Williams, 1991). In brief, spectra were transferred to a PC-486 computer from the spectrometer photodiode interface via a direct memory access (DMA) unit in order to allow for the high data transfer rates required for spectrum-imaging. The PC also controlled the STEM deflection coils so that the probe could be digitally rastered on the specimen. The spectrum-images were stored on disk and then backed up on DAT tape; a non-compressed 128x128 pixel EELS-image required 32 Mbytes of storage. Annular dark-field images could also be acquired digitally by feeding single pulses generated by a YAG scintillator, photomultiplier and discriminator/amplifier into a fast counter in the computer. This enabled a 512x512 pixel dark-field image to be recorded in approximately 25 s at very low electron dose. Alternatively, dark-field images could be acquired at higher electron doses by digitizing the analog output of the photomultiplier. The images were transferred to an Apple Macintosh II computer for analysis by means of the image processing program, IMAGE, written at NIH by W.S. Rasband (O'Neill *et al.*, 1989). EELS spectrum-images were processed by specially designed software running on the PC.

Advantages of EELS for Biological Microanalysis

EELS has a number of important advantages compared with EDXS. In particular, the technique is sensitive to the light element K-edges for which the X-ray fluorescence is very low (Isaacson and Johnson, 1975; Colliex, 1984; Egerton, 1986; Leapman, 1979). Additionally, the typical spectrometer acceptance angle of 0.02 radians gives a high collection efficiency for EELS (generally greater than 50%) since the fast electrons are inelastically scattered in the forward direction (for primary energy $E_0 = 100$ keV and energy losses of $0.2 \text{ keV} < \Delta E < 2 \text{ keV}$ the angular distribution has half-angle $\beta = \Delta E/2E_0 = 0.001$ to 0.01 rad). By comparison, the collection solid angle for an EDXS detector is typically no better than 0.2 steradians, and the characteristic X-rays are emitted uniformly into 4π steradians yielding a geometric efficiency of about 2%. On the other hand, EELS is also limited in certain respects.

An important requirement is that specimens must be suitably thin, otherwise the signal is degraded by plural scattering effects (Egerton, 1986; Leapman and Swyt, 1981). In practice the thickness should not exceed a limit of between 0.5 to $1.0\lambda_i$, where λ_i is the inelastic mean free path which depends on the specimen density (λ_i is approximately 80 nm for an equivalent carbon film at 100 keV beam energy). It should be noted that, since about 30% of the cryosectioned tissue mass is lost on irradiation, the initial thickness can be somewhat greater. Furthermore, between typically 50% and 90% of the hydrated cryosection mass is water. After dehydration we therefore expect a 100 to 200 nm cryosection to be just thin enough for analysis at 100 keV. This has been confirmed experimentally (Buchanan *et al.*, 1993), although there may sometimes be an advantage in operating at 200 keV beam energy.

A more fundamental limitation is that the energy loss spectrum suffers from a large background intensity originating from the tails of lower energy core-edges and other inelastic processes (e.g., valence electron excitations). Indeed, although theory had originally predicted that small mass fractions should be detectable (Isaacson and Johnson, 1975), it was generally believed that EELS offered a poorer fractional sensitivity than EDXS for most heavier elements. Later it was appreciated that, like X-ray absorption spectra, the EELS core-edges of certain elements are distinguished by the presence of so-called "white-line" resonances at the L_{23}-edges originating from high densities of unoccupied states (Ahn and Krivanek, 1983). One of the most favorable of these elements is calcium. The calcium ion is particularly important biologically because it serves as an intracellu

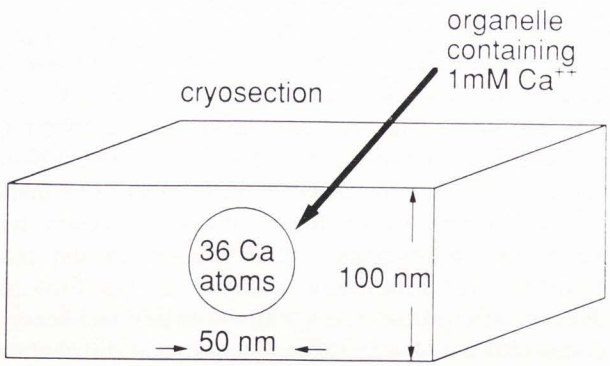

Figure 2: Diagram indicating 50-nm diameter organelle in 100-nm thick cryosection: calcium concentration of 1mM corresponds to only 36 Ca atoms.

lar second messenger for many cellular functions. Whereas other biological elements such as sodium, potassium, chlorine, phosphorus and sulfur are generally present at the 5 to 100 millimolar (mM) level and are therefore relatively easy to measure by EDXS, detection of calcium is a challenging task because physiological concentrations of this element are typically in the sub-millimolar range (Somlyo *et al.*, 1985). For example, a spherical organelle of diameter 50 nm with a 1 mM concentration of Ca^{2+} contains on average only 36 calcium atoms (see Figure 2). Moreover, we should like to detect changes of the order of 10% which corresponds to variations of only a few atoms in the organelle. The data acquisition times needed for many microanalytical studies often depend on obtaining sufficient counting statistics to detect the low calcium concentrations and even if EELS were used solely for this element the advantages would be considerable.

Acquisition and Processing Techniques

Although theory tells us to expect a favorable signal/noise for detection of trace elements like calcium (Isaacson and Johnson, 1975; Leapman, 1992), the raw parallel EELS spectrum only reveals the presence of the major elements, carbon, nitrogen, and oxygen. In fact, we can predict that the signal/background ratio at the calcium L_{23}-edge will typically be below 0.1% for physiological concentration in the millimolar range. The signal of interest is therefore hidden and special acquisition and processing techniques must be employed to extract it. It is important to take account of the various detector noise terms.

Consider a flux N_i of electrons incident at the YAG scintillator in the vicinity of one photodiode array channel so that the associated shot noise in the beam is: $n_s = \sqrt{N_i}$. As has been recently pointed out by Egerton *et al.* (1992), the signal is actually smoothed out over several channels by electron or light scattering in the scintillator according to the point-spread function of the detector. The observed shot noise, $n_s' = \sqrt{N_i}/s$, is therefore also smoothed out by a factor of s, which in our system is around 3. If there were no additional noise contributions the apparent signal/noise ratio would then be given by: $SNR_{in} = N_i / n_s = s\sqrt{N_i}$. However there are two other significant sources of noise. One originates from the detector electronics and increases with the number of read-outs, p, of the photodiode array. This read-out noise, n_r, is given in terms of an equivalent number of incident electrons and in our system has a value of approximately 60. The other is pattern noise due to channel-to-channel gain variations between the individual photodiode elements. It contributes a constant fraction, v, of the incident flux. By adding these three terms in quadrature we obtain a measured output signal/noise ratio (Krivanek *et al.*, 1987; Egerton *et al.*, 1992) given by:

$$SNR_{out} = \frac{N_i}{\sqrt{pn_r^2 + s^{-2}N_i + v^2N_i^2}} \qquad (1)$$

The detective quantum efficiency (DQE) is defined as:

$$DQE = \left[\frac{(SNR)_{out}}{(SNR)_{ins}}\right]^2 \qquad (2)$$

which can therefore be expressed as:

$$DQE = \frac{N_i}{s^2\left[pn_r^2 + s^{-2}N_i + v^2N_i^2\right]} \qquad (3)$$

From the form of Eq. (3) we can see that the DQE is maximized by decreasing the number of read-outs, p, until the total incident light almost fully discharges each photodiode element. In the Gatan system saturation occurs at $2^{14}=16384$ photodiode counts which corresponds to about 6×10^5 incident electrons. This condition of large (almost saturating) values of N_i is easily satisfied for biological microanalysis at energy losses below 500 eV in the field-emission STEM. If it were not for the pattern noise term a DQE of between 0.2 and 0.5 would then be obtainable. However, the channel gain typically has a root mean square variation of around $v \approx 0.5\%$ which completely masks the signal that is over ten times smaller. Fortunately, there are several

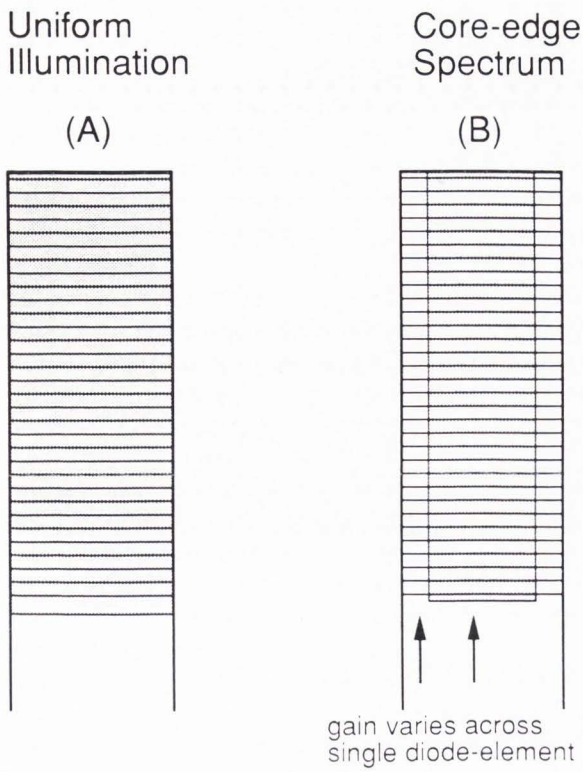

Figure 3: Schematic diagram showing energy loss spectrum on photodiode array under conditions of (A) uniform illumination with broad-beam dispersion setting, and (B) scanned core-edge spectrum. Array elements not drawn to scale –actual width/height ratio is 100:1.

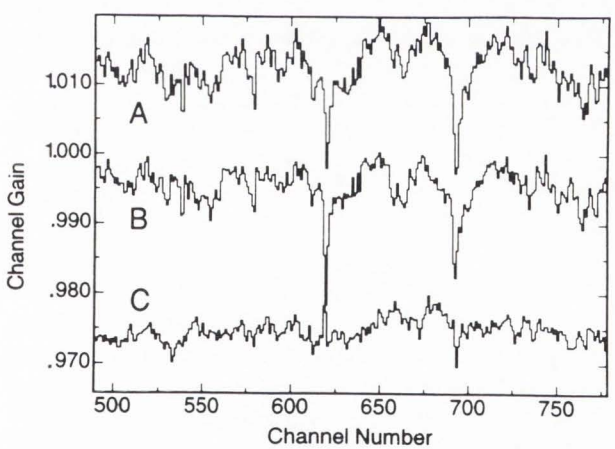

Figure 4: Detector channel-to-channel gain function obtained (A) by broad-beam uniform illumination and (B) by scanning core-edge across photodiode array. Curve (C) is result of dividing A by B and shows residual channel gain function when method A is used.

ways of reducing the effects of these channel-to-channel gain variations.

The most straightforward method for reducing effects of gain variations is to divide the spectrum by a normalized response function obtained by exposing the photodiode array to broad beam illumination, which in the Gatan system can be achieved by using a special setting of the dispersion lenses. In practice, it is found that the gain function so obtained is not quite correct because of variations in sensitivity perpendicular to the dispersion direction due, for example, to imperfections in the YAG scintillator. This spectral width perpendicular to the dispersion direction changes according to the region of the energy loss spectrum. The width of each photodiode element is 2.5 mm compared with a diode spacing of only 25 μm, as shown schematically in Figure 3. A better representation of the gain function can be obtained by scanning a featureless region of the spectrum over the detector array. Although both methods give similar results (Figure 4: curves A and B), a significant residual channel-to-channel gain is evident after correcting by the detector response using the broad beam illumination (Figure 4: curve C). The noise reduction obtained with the improved scanning method is illustrated in Figure 5a where it is applied to a core-edge spectrum recorded from a mitochondrion in a dendrite of a cryosectioned neuron. The same spectrum is shown in Figure 5b after a first-difference digital filter has been used to enhance weak spectral features. Channel-to-channel gain variations are now corrected to within about $\pm 0.05\%$ which is adequate for certain applications. Nevertheless, a small fraction of pattern noise still remains and this can interfere with detection of the extremely weak Ca edge.

An alternative approach for detecting such small signals is to use the difference acquisition method developed by Shuman and Kruit (1985) and by Shuman and Somlyo (1987). The first-difference spectrum is obtained by acquiring two spectra shifted electrically over the photodiode array by energies $-\Delta/2$ and $+\Delta/2$. If the spectral intensity at channel n corresponding to energy E_n is $I(E_n)$ then the first difference spectrum is given by,

$$I'(E_n) = I(E_n + \Delta/2) - I(E_n - \Delta/2) \qquad (4)$$

This operation is similar to a first derivative and it enhances small spectral features situated on a large slowly-varying background. To optimize the signal-to-noise ratio in the first-difference spectrum we should set Δ to be somewhat greater than the energy width of the

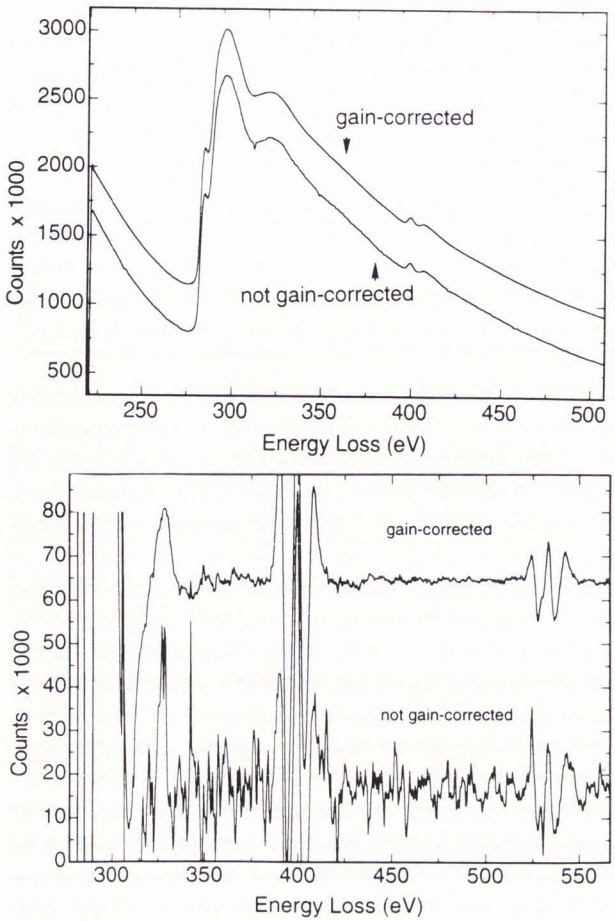

Figure 5: Gain-corrected and uncorrected core-edge spectra from cryosectioned mitochondrion in neuron. (a) normal spectrum, (b) digitally-filtered first-difference.

feature. For example if we wish to detect a weak Ca L_{23} edge we should select Δ about 6 eV, the measured width of the pair of white lines being approximately 4 eV. The most important advantage, in addition to enhancing edge visibility, is that the gain fluctuations in $I'(E_n)$ are greatly reduced because we are subtracting two nearly equal spectra each with the same channel gain variations.

Sometimes it is useful to obtain a second-difference spectrum by collecting three spectra offset electrically by energies $-\Delta$, 0, and $+\Delta$,

$$I''(E_n) = I(E_n) - [I(E_n + \Delta)]/2 - [I(E_n - \Delta)]/2 \qquad (5)$$

This is similar to a negative second-derivative and can be easier to interpret than the first-derivative since a peak in the normal spectrum appears as a peak in the second difference spectrum. These difference spectra can be acquired very easily and, although they may appear more complicated, quantification can be accomplished. The main disadvantage of this approach is that the detective quantum efficiency is effectively decreased by a factor of two (for first-difference spectra) or three (for second-difference spectra). Recent papers by Wang *et al.* (1992) and by Bonnet *et al.* (1992) discuss in detail the optimal parameters for difference acquisition. Iterative schemes for reduction of detector gain variations have also been developed (Schattschneider and Jonas, 1993).

The use of difference spectrum acquisition to remove channel gain variations is only necessary for one-dimensional detectors. For two-dimensional CCD arrays the gain variations can be compensated exactly by dividing by the complete two-dimensional detector response (Zaluzec and Strauss, 1989; Krivanek and Mooney, 1993). A filter of optimal width can then be applied to extract small signals, with the advantage of retaining the raw data. In any case, to quantify the difference (or filtered) spectra it becomes necessary to fit reference spectra obtained from standards. This may be complicated for a general analysis problem because the detailed core edge shape can vary depending on the type of chemical bonding. Fortunately, the Ca L_{23} excitation is dominated by a white line resonance and its edge shape does not vary significantly from specimen to specimen. A calcium reference spectrum can simply be generated, for example, from a specimen of calcium chloride deposited on a thin carbon film, and the background can be approximated by a spectrum recorded from a thin carbon film. In general, double scattering must also be taken into account as discussed by Shuman and Somlyo (1987). This can be accomplished by convolving the carbon single scattering (low-loss) spectrum with the core-edge from a thin carbon film (Leapman *et al.*, 1993).

To see how the fitting procedure works in practice for calcium analysis, consider a region of a first-difference core-edge spectrum $I'(E_n)$ containing N channels with energies E_n, and assume that the spectrum is the sum of the calcium reference spectrum $X_{Ca}(E_n)$ as well as contributions from the background $X_m(E_n)$, where m=1 to M, and M is the number of reference spectra included for the background. We can then determine the fitting coefficient a_{Ca} by minimizing the value of c^2 using a multiple least squares procedure,

$$\chi^2 = \sum_{n=1}^{N} \left[[I'(E_n) - a_{Ca} X_{Ca}(E_n) - \sum_{m=1}^{M} a_m X_m(E_n)]^2 / [\sigma(E_n)]^2 \right]$$

$$= minimum \qquad (6)$$

where $\sigma(E_n)$ is the estimated standard error in the n^{th} channel of the unknown spectrum. Quantitative results

can then be obtained from the fitting coefficients if the first-difference reference spectrum is normalized to the integrated counts for some energy window Δ above the edge. The integrated edge intensities are easily obtained by means of the conventional inverse power law background extrapolation. If $I_{Ca}^{ref}(E_n)$ is the measured number of counts in the calcium reference spectrum, and $S_{Ca}^{ref}(\Delta,\beta)$ is the integrated signal in energy window Δ for collection angle β, then the first-difference calcium reference spectrum $I'_{Ca}{}^{ref}(E_n)$ can be normalized as follows (Leapman, 1992),

$$X_{Ca}(E_n)=I'^{ref}_{Ca}(E_n)/S^{ref}_{Ca}(\Delta,\beta) \qquad (7)$$

The fitting coefficient is now equal to the estimated integrated core edge intensity, i.e., $a_{Ca} = S_{Ca}(\Delta,\beta)$. A quantitative estimate for the atomic fraction of calcium to carbon, N_{Ca}/N_C , can then be obtained from the integrated carbon K-edge signal,

$$N_{Ca}/N_C=[a_{Ca}/S_C(\Delta,\beta)][\sigma_C(\Delta,\beta)/\sigma_{Ca}(\Delta,\beta)] \qquad (8)$$

where $\sigma_{Ca}(\Delta,\beta)$ and $\sigma_C(\Delta,\beta)$ are the respective partial ionization cross section for calcium and carbon. Since the dry weight fraction of carbon in proteins is typically 55% and protein is the major organic component of dried tissue, we can estimate the molar concentration of calcium from the Ca/C ratio.

Calcium Detection in Cryosectioned Cells

We have used EELS to measure low calcium concentrations in brain where calcium is essential in the modulation of neuronal activity (Andrews *et al.*, 1988). Figure 6 shows a digital dark-field STEM image from a region of rapidly frozen and cryosectioned mouse cerebellar cortex containing a number of Purkinje cell neurons (also see: Andrews *et al.*, 1994). An energy loss spectrum recorded from a cistern of dendritic endoplasmic reticulum about 30 nm in diameter is shown in Figure 7a. This spectrum was acquired with a beam current of 5 nA in approximately 100 s, and with a collection semi-angle referred to the specimen of 20 mrad which included most of the Ca L_{23}-edge signal. Although only the major elements, carbon and nitrogen, are visible in the normal spectrum, use of the first-difference acquisition with Δ = ±3 eV easily reveals the weak calcium L_{23}-edge at 348 eV which is only 0.1% of the background intensity. Quantification of the calcium signal was achieved by fitting reference spectra

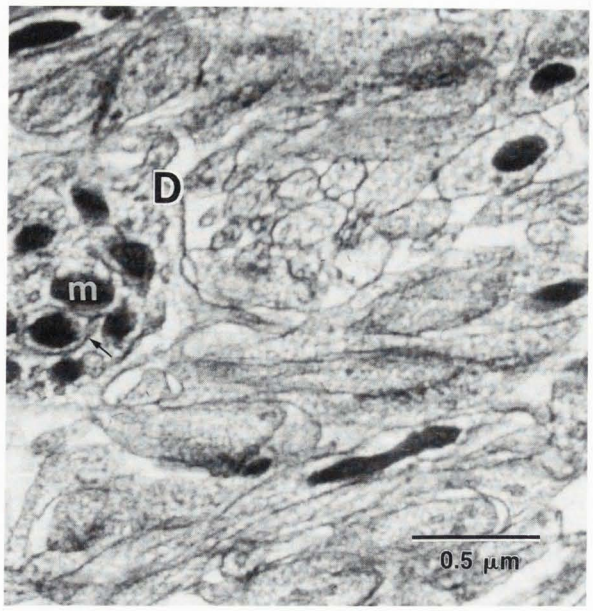

Figure 6: Digital dark-field STEM image from region of rapidly-frozen and cryosectioned mouse cerebellar cortex containing Purkinje cell neurons. Dendrite (D) contains mitochondria (M) and endoplasmic reticulum (arrows).

from $CaCl_2$ using the multiple least squares method discussed above. A carbon film spectrum served as a reference spectrum for the background produced by the matrix and a plural scattering reference term was included to take account of thickness variations. The computed Ca/C atomic fraction of 1.1 ± 0.2 $x10^{-4}$ translates into a Ca concentration of 5.0 ± 0.8 mmol/kg dry weight and corresponds to less than 100 Ca atoms in the analytical volume. Although the cisterns of ER were oriented with the membranes nearly perpendicular to the plane of the cryosection, some contribution from the surrounding cytoplasm was likely to have occurred in the analysis. Figure 7b compares the energy-dispersive X-ray spectrum recorded under equivalent dose conditions from a similar region of endoplasmic reticulum. The EDXS detector has an ultrathin window and subtends a solid angle of 0.18 sterad — and so represents a relatively well optimized system. Although major elements (P, S, Cl and K) are easily visible in the X-ray spectrum, the estimated calcium sensitivity of ± 3 mmol/kg (± standard deviation) is about four times lower than for EELS in agreement with earlier predictions. These results demonstrate the complementary advantages of EELS and EDX for elemental analysis.

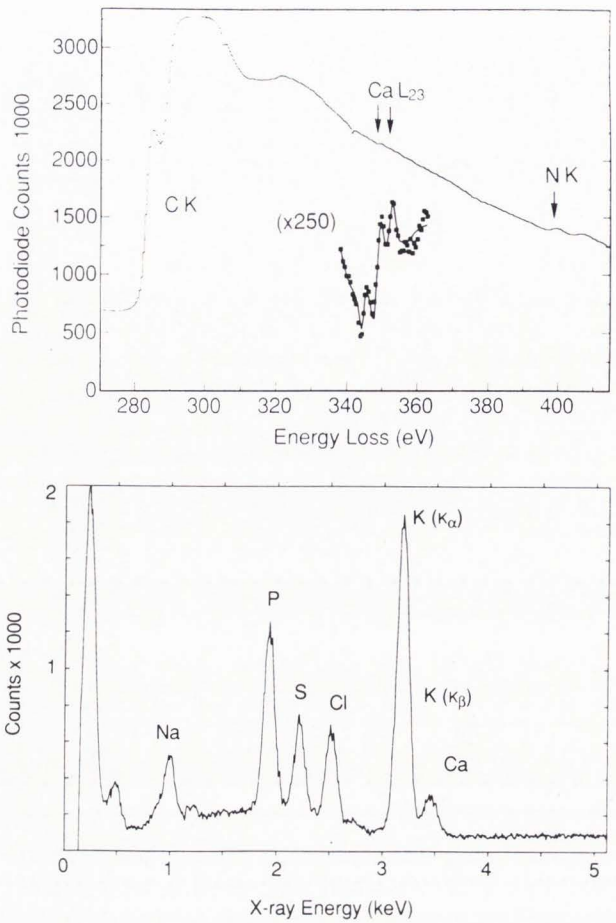

Figure 7: (a) EELS from cistern of dendritic endoplasmic reticulum similar to that in Figure 6. Inset: first-difference acquisition ($\Delta E = 6eV$) shows detection of 5 mmol/kg of calcium. (b) energy-dispersive X-ray spectrum recorded under equivalent dose conditions.

Elemental Mapping

In addition to acquiring EELS data from a point in the specimen we can obtain images representing the elemental distributions by digitally scanning the probe and recording entire spectra in parallel at each pixel, a technique referred to as spectrum-imaging (Jeanguillaume and Colliex, 1989; Hunt and Williams, 1991; Balossier *et al.*, 1991; Leapman and Hunt, 1992). This approach is equivalent to the EDXS mapping techniques that have also been recently implemented. The spectrum-imaging approach is also complementary to energy-filtered imaging in which entire inelastic images are recorded in parallel by means of a two-dimensional detector (e.g., CCD array) but in which the spectral information must recorded serially one energy loss at a time (Krivanek *et al.*, 1992; Lavergne *et al.*, 1992; Körtje, 1994). Energy-filtered imaging has a significant advantage when data from large numbers of pixels are required, e.g., a 512x512 pixel spectrum-image would take two hours to acquire with a typical minimum integration time of 25 ms per pixel, whereas it might only take a few seconds in the energy-filtering microscope (e.g., Ottensmeyer, 1984). However, the STEM spectrum-imaging approach is essential for applications involving detection of physiologically relevant concentrations of calcium in rapidly-frozen, cryosectioned tissue. This is because very precise background modeling must be used to extract the very weak signal. In the energy-filtering technique the post-edge background can only be extrapolated from other pre-edge images so that limited precision is available.

We have applied parallel-EELS mapping to the analysis of Purkinje cell dendrites mentioned in the previous paragraph (also see: Leapman *et al.*, 1993). Two spectra, shifted in energy by $\pm$ 3 eV, were acquired at each pixel with a total recording time of approximately 1600 s (corresponding to a dwell time of 0.4 s per pixel). In this way it was possible to obtain both conventional core-edge intensity maps as well as difference-spectra from specific regions of the specimen. A nitrogen map was first generated by subtracting the background under the K-edge as shown in Figure 8b; this provided structural information about the distribution of proteins. By comparing the nitrogen map with the corresponding dark-field image (Figure 8a) recorded at low dose, it was possible to segment the EELS map into separate binary masks consisting of mitochondria and ER (Figs. 8c and 8d). This segmentation was simply performed by outlining the masked regions using image processing software. The first-difference spectra from four segmented 64x64 pixel spectrum-images were then summed in order to improve the counting statistics. Although the calcium signal was easily visible in this summed first difference spectrum, a 10eV wide high pass filter was used to reduce the residual background intensity. The shape of the narrow L_{23} white line feature was not strongly affected by this operation, and the spectra could be quantified because the reference spectra were filtered in the same way. After the processing had been carried out the spectra in Figure 9a and 9b were obtained for ER and mitochondria respectively. Quantitation of these spectra gave calcium concentrations of 4.9 $\pm$ 0.4 and 1.4 $\pm$ 0.4 mmol/kg dry weight in endoplasmic reticulum and mitochondria, respectively.

The shorter acquisition times for EELS coupled with the spectrum-imaging capability make it more feasible to sample exhaustively structures such as the Purkinje cell dendrites considered in this work. Using segmentation methods it then becomes possible to correlate changes that occur within a given structural unit, e.g., increase

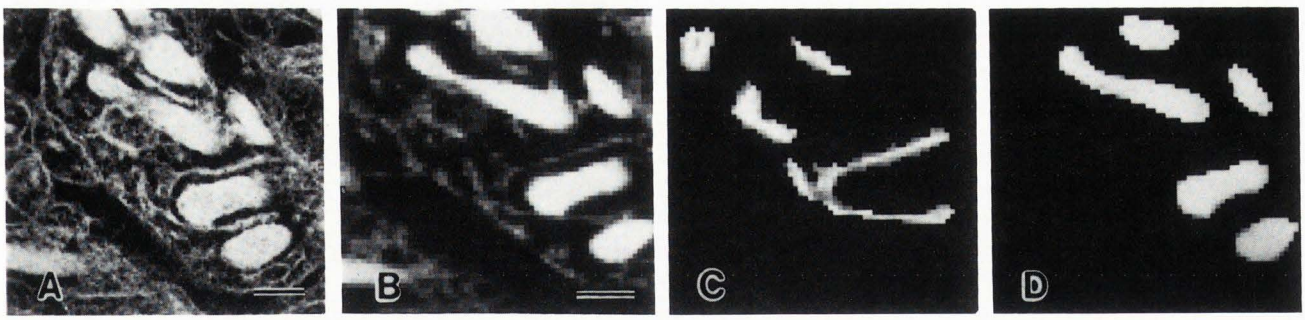

Figure 8: Parallel EELS maps of Purkinje cell dendrite in mouse cerebellar cortex: (a) low-dose dark-field image, (b) nitrogen K-edge map, and segmentation into (c) endoplasmic reticulum and (d) mitochondria. Bar = 200 nm.

in cytoplasmic calcium with a decrease in ER calcium. Although the required electron dose is less than for EDXS, little advantage is expected in terms of radiation damage since the EELS dose of about 10^8 e/nm^2 is still very high and produces terminal mass loss in the specimen anyway.

Phosphorus Detection in Macromolecular Assemblies

The high elemental sensitivity offered by EELS can also be applied to the analysis of isolated, rapidly-frozen macromolecular assemblies (Leapman and Andrews, 1992). Although the elemental analysis must be carried out at high electron dose and therefore inevitably results in radiation damage, the EELS measurements can be made after low-dose STEM dark-field imaging so that macromolecules can be characterized in terms of their molecular weight distributions. Phosphorus is a particularly important element for this type of analysis since it provides information about the nucleic acid content of protein/nucleic acid complexes, as well as information about the phosphorylation state of, for example, cytoskeletal and regulatory proteins.

We can illustrate how phosphorus detection can be achieved by considering the analysis of tobacco mosaic virus (TMV). TMV is rod-shaped having a molecular weight of 39 Md, a length of 300 nm and a diameter of 18 nm. The virus contains a single strand of RNA with approximately 6600 bases, so there are approximately 22 phosphorus atoms per nanometer along the length of the molecule. Figure 10a shows a typical dark-field STEM image of several TMV particles recorded at a dose of 10^3 e/nm^2. Normal and second-difference EELS spectra from a 10 nm x 10 nm area in the center of the virus were obtained with a probe current of 1nA and an acquisition time of 150 s (Figure 10b). Although no phosphorus edge is observed in the normal spectrum, the phosphorus L_{23}-edge at 132 eV is clearly visible in the second-difference spectrum. This corresponds to detection of approximately 200 phosphorus atoms in the analytical volume. It would be very difficult to detect such a low concentration by energy filtering because the signal/background is only around 1% and the signal lies on a rapidly varying background. It has been proposed phosphorus mapping should be feasible at low dose if the characteristic core loss signal is averaged over many identical macromolecular assemblies in a periodic crystalline array, e.g., reconstituted membranes containing protein and phospholipid moieties (Reichelt *et al.*, 1986). In the case of a filamentous structure like TMV, the radial elemental distribution could be determined by averaging along its length.

Other bound atoms have also been detected in metalloproteins by STEM / parallel-EELS and a sensitivity near the single atom level has been demonstrated (Leapman and Andrews, 1992; Krivanek *et al.*, 1991). This is illustrated in Figure 11 which shows the detection of four iron atoms in a single molecule of hemoglobin. An extremely high dose is necessary ($>10^{10}$ e/nm^2) to achieve this sensitivity. Although the analysis is found to be highly destructive under these conditions (probably as a result of displacement or "knock-on" damage) the atoms of interest seem to stay in the specimen at least when cooled to liquid nitrogen temperature.

Water Measurements by Valence EELS

So far we have considered only information that originates from the core-edge spectrum. The valence excitation spectrum, which includes energy losses in the range from zero to roughly 50 eV, has a much higher cross section than the inner shell excitations. However, the low-loss spectrum is much more complicated and, for biological specimens, the expected variations due to

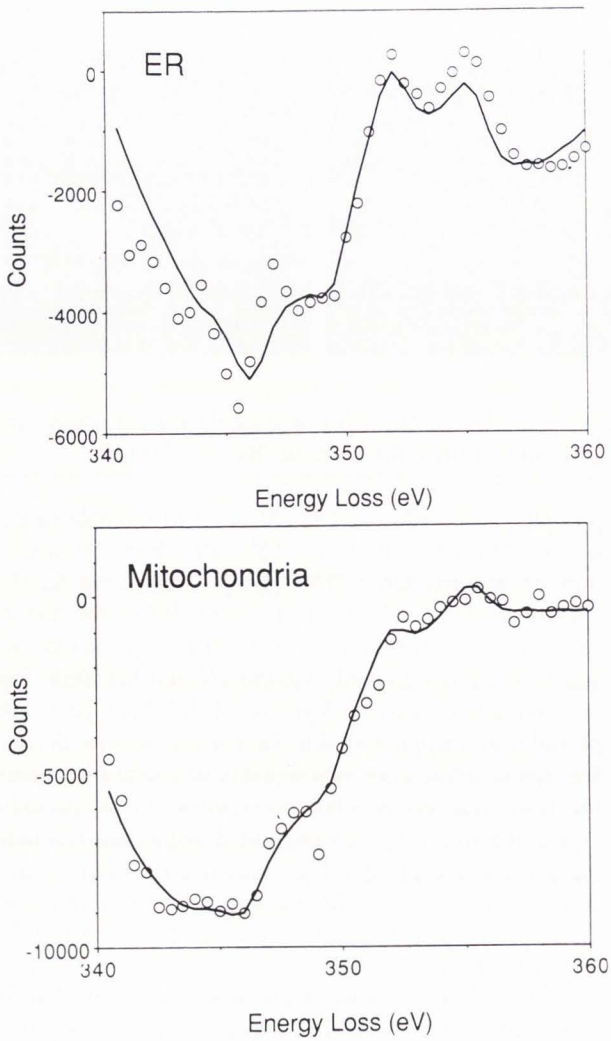

Figure 9: Summed difference-spectra from four EELS-images of Purkinje cell dendrites: (a) endoplasmic reticulum and (b) mitochondria.

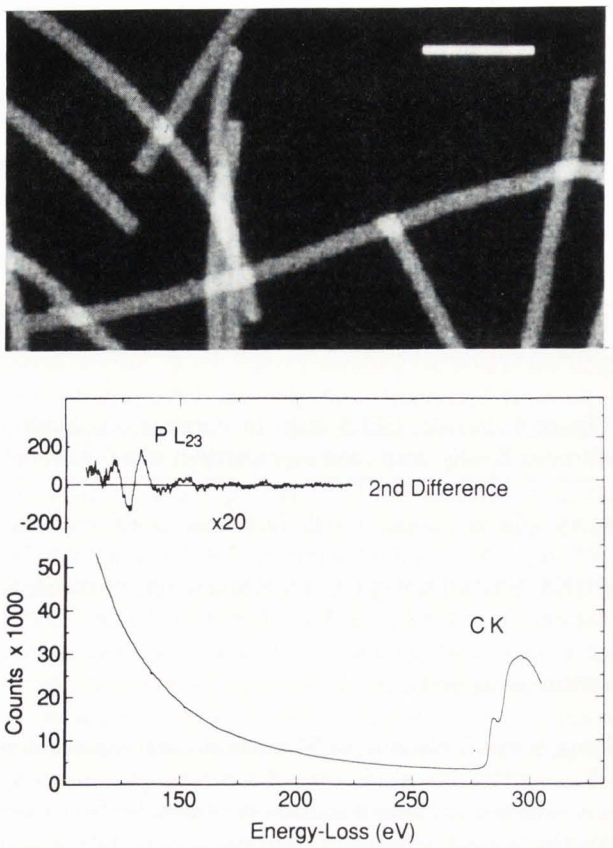

Figure 10: (a) Dark-field STEM image showing field of tobacco mosaic virus (TMV) particles. Bar = 100 nm. (b) Normal and second-difference spectra (Δ=6 eV) recorded from 10-nm diameter region in center of TMV.

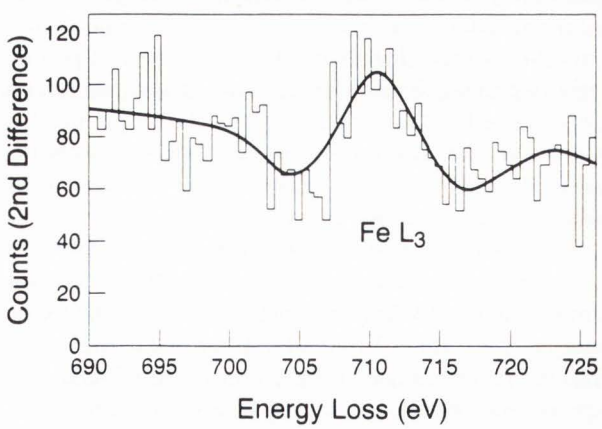

Figure 11: Parallel EELS from single hemoglobin molecule showing detection of four iron atoms; fitted curve is reference spectrum obtained from ferritin molecule.

compositional differences are more subtle (Egerton, 1986). The valence spectrum is dominated by a collective plasmon excitation at around 20 eV but also contains molecular excitations at energy losses of around 4 to 12 eV. Previously, the main use of the low-loss spectrum in biological microanalysis has been to assess the specimen thickness through the relation:

$$t=\lambda_i \ln(I_{tot}/I_o) \qquad (9)$$

where I_o is the zero-loss intensity, I_{tot} is the total integrated intensity in the spectrum, and λ_i is the inelastic mean free path. This expression can be applied to estimate the thickness of frozen-hydrated cryosections. It has been determined that the mean free path for water at 100 keV beam energy is 210 nm (to within an accuracy of 5%) assuming a density of 0.93 for ice (Sun *et al.*, 1993); and the mean free path for hydrated tissue has approxi-

mately the same value.

By taking advantage of (i) the higher energy resolution available with the field-emission source, (ii) an efficient parallel detection system and (iii) a stable cryotransfer stage for the STEM, it has become possible for the first time to exploit the detailed information contained in the low-loss spectrum to characterize frozen hydrated biological specimens. In particular, the valence excitation technique provides a practical basis for determining the fraction of water in an organelle (Sun *et al.*, 1993). The water content of subcellular compartments is an important physiological quantity that reflects how fluid and electrolyte concentrations are regulated both indirectly by osmotic effects following ion movements and directly through water-specific membrane channels. Previously, analytical electron microscopy has provided only an indirect determination of the subcellular water content in thin tissue sections because the measurements have been made after dehydration (e.g., von Zglinicki, 1991; Gupta and Hall, 1981; Zierold, 1988; Leapman and Ornberg, 1988; Buchanan *et al.*, 1993).

The basis for the EELS water determination is evident in Figure 12 which shows that significant differences exist between the energy loss spectra of water and protein. We see that the spectrum from ice has a plasmon maximum at 20.4 eV compared with 23.4 eV for the protein. Additionally, at lower energies the spectrum from ice contains zero intensity until a peak occurs at 9.1 eV which can be attributed to excitation of electrons across the band-gap, whereas a weaker peak at 6.7 eV in the protein can be attributed to excitation of π-states.

It is assumed that the main contributions to the low-loss fine structure are due to intramolecular bonding and the interaction between these basic constituents are relatively unimportant. To determine the water mass fraction in an unknown specimen we simply model its spectrum by expressing it as a linear sum of contributions from the constituent compounds. The spectra from these components can thus be treated as standard refer ence spectra and the coefficients can be determined by MLS fitting as described above for core-edge quantitation. First, we must remove effects of plural inelastic scattering by deriving the single-scattering distributions using the Fourier-logarithmic deconvolution procedure. The single scattering distribution, $S^h(E)$, from the hydrated specimen is now given in terms of the single scattering distributions for the different components, $S_i(E)$, and the fitting coefficients, a_i, by the sum,

$$S^h(E)=\sum_{i=1}^{M} a_i S_i(E) \qquad (10)$$

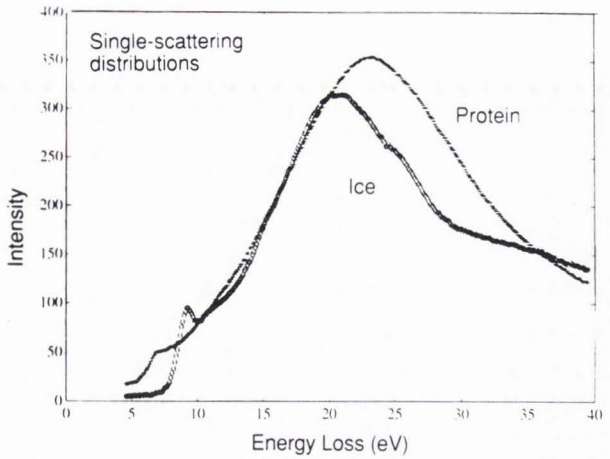

Figure 12: Single-scattering distributions recorded at dispersion of 0.1 eV/channel from ice and from bovine serum albumin.

In Eq. 10 all spectra have been corrected for the support film by subtracting an appropriate fraction of the carbon single-scattering distribution.

In practice, we find that the experimental spectra can be modeled very well by a linear combination of just the protein and ice spectra, because protein is the major organic constituent. This can be generalized to take account of other organic constituents in the specimen such as nucleic acids, carbohydrates, and lipids by including additional reference spectra as indicated. We find that the mass fraction of water f_{water} is given by,

$$f_{water}=\left[1+k\frac{a_{protein}}{a_{water}}+\ldots\right]^{-1} \qquad (11)$$

where k is the ratio of cross section per unit mass for water to that for protein. Our earlier work (Sun *et al.*, 1993) has shown that k has a value of 0.89 ± 0.03.

As an example we have applied the valence EELS technique to estimate the water content of a micrometer-diameter region of neuropil in a frozen-hydrated cryosection of cerebellar cortex, similar to the section shown dehydrated in Figure 6. By fitting the reference spectra (Figure 12) to the single-scattering distribution in Figure 13 we obtain an estimated water content of 78 ± 3 %, which is consistent with the expected value of around 80%. The spatial resolution for the water measurements is limited by radiolytic damage in the electron beam. Experimentally we find that approximately 10^5 photodiode counts are required in the entire energy loss spectrum ($\sim10^7$ primary electrons) in order to obtain acceptable statistical errors in the MLS fitting. This electron flux will provide around ±5% uncertainty in a

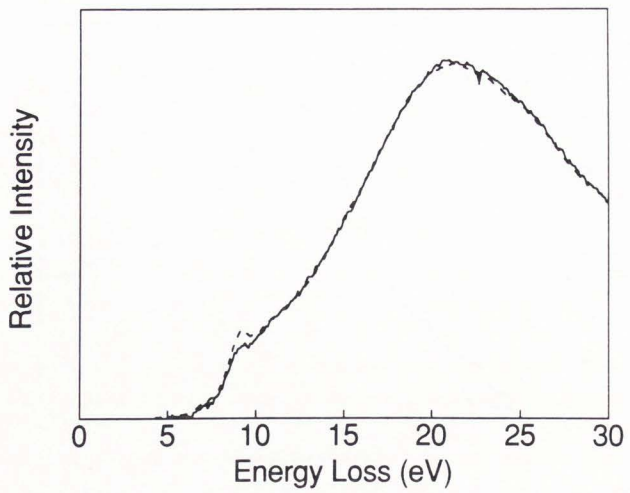

Figure 13: Single-scattering distribution from 1-μm diameter region of frozen-hydrated neuropil in cryosectioned mouse cerebellar cortex (solid curve). Fit to water and protein reference spectra (dashed curve) gave water content of 78 ± 3 %.

single measurement. Given a maximum allowed dose of around 10^3 e/nm^2 (Dubochet *et al.*, 1988; Isaacson, 1977), the minimum diameter of the specimen that can be analyzed is 100 nm. Such a scale provides a useful resolution for analysis of hydrated cryosections; it is commensurable with the specimen thickness and also with the sizes of all but the smallest organelles. Higher resolution or greater precision in the EELS water measurement can be achieved by averaging spectra over many identical structures in the specimen.

It is now possible to acquire valence EELS-images that can provide two-dimensional maps of the water distribution in a frozen-hydrated section (Leapman and Sun, unpublished results). Cryosectioned tissue normally appears featureless in the analytical electron microscope apart from artifacts due to compression, knife marks, or adventitious ice contamination. The EELS water images thus reveal entirely new contrast information that remains concealed in conventional imaging modes.

Conclusions

Instrumentation and processing techniques for EELS in the field-emission STEM have now been developed to the stage where interesting biological applications have become feasible. Parallel EELS provides an improvement in sensitivity by a factor of three or four relative to EDXS for calcium detection. Due to advances in cryosectioning, this advantage can be realized even in a 100 keV instrument. This capability of EELS is particularly significant because calcium is a very important element that is often present at levels that are only just detectable by EDXS. Spectrum-imaging allows maximum flexibility in processing the data and segmentation techniques can be used to select the analysis region after acquisition. The main difficulty with EELS data is the small core-edge signal/background ratio that requires special processing techniques such as difference-acquisition and digital filtering. Some refinements may still be needed to improve the background correction. Parallel EELS in the field-emission STEM offers extremely high sensitivity, and near single atom detectability has been obtained in the analysis of macromolecular assemblies. EELS also has a particularly high sensitivity for phosphorus which can provide information about protein phosphorylation and the composition of protein-nucleic acid complexes. Although such measurements must be recorded at high electron doses and are therefore susceptible to beam damage, structures can be characterized by low-dose STEM imaging prior to analysis. Finally, detailed information obtained from the valence excitation spectrum can be used to measure the water content in subcellular compartments of frozen-hydrated cryosections at a resolution of around 100 nm. Development of this technique in the future should allow direct water mapping of hydrated tissue.

References

Ahn CC, Krivanek OL (1983) EELS Atlas, ASU Center for Solid State Science, Tempe, AZ; and Gatan Inc., Warrendale, PA.

Andrews SB, Buchanan RA, Leapman RD (1994) Quantitative dark-field mass analysis of ultrathin cryosections in the field-emission STEM. Scanning Microscopy Supplement.

Andrews SB, Leapman RD, Landis DMD, Reese TS (1988) Activity-dependent accumulation of calcium in Purkinje cell dendritic spines. Proc Natl Acad Sci USA **85**: 1682-1685.

Andrews SB, Leapman RD (1989) Performance of a cryotransfer/cold stage system for a VG Microscopes HB501 STEM. In: *Microbeam Analysis 1989* (Russell PE, ed) San Francisco Press, San Francisco, pp 85-88.

Balossier G, Thomas X, Michel J, Wagner D, Bonhomme P, Ploton D, Bonhomme A, Pinon JM (1991) Parallel EELS elemental mapping in scanning transmission electron microscopy: use of the difference methods. Microsc Microanal Microstruct **2**: 531-546.

Bonnet N, Michel J, Wagner D, Balossier G (1992) Optimization of digital filters for the detection of trace elements in electron energy loss spectroscopy. I Theory and simulations. Ultramicroscopy **41**: 105-114.

Buchanan RA, Leapman RD, O'Connell MF, Reese

TS, Andrews SB (1993) Applications of the field-emission STEM to subcellular structure and analysis of ultrathin tissue cryosections. J Struct Biol **110**: 244-255.

Colliex C (1984) Electron energy loss spectroscopy in the electron microscope. In: *Advances in Optical and Electron Microscopy* (Cosslett VE, Barer R, eds) Academic Press, London, Vol 9, pp 65-177.

Crewe AV (1970) The current state of high-resolution scanning electron microscopy. Quart Rev Biophys **31**: 137-175.

Dubochet J, Adrian M, Chang J, Homo J-Cl, Lepault J, McDowall AW, Schultz P (1988) Cryo-electron microscopy of vitrified specimens. Quart Rev Biophys **21**: 129-228.

Egerton RF (1986) *Electron Energy Loss Spectroscopy in the Electron Microscope*, Plenum, New York, pp 1-25.

Egerton RF, Yang Y-Y, Cheng SC (1993) Characterization and use of the Gatan 666 parallel-recording electron energy-loss spectrometer. Ultramicroscopy **48**: 239-246.

Engel A (1978) Molecular weight determination by scanning transmission electron microscopy. Ultramicroscopy **3**: 273-281.

Gupta BL, Hall TA (1981) The X-ray microanalysis of frozen-hydrated specimens in scanning microscopy: an evaluation. Tissue Cell **13**: 623-643.

Hunt J, Williams DB (1991) Electron energy-loss spectrum-imaging. Ultramicroscopy **38**: 47-73.

Isaacson MS, Johnson D (1975) Low Z elemental analysis using energy loss electrons. Ultramicroscopy **1**: 33-52.

Isaacson MS (1977) Specimen damage in the electron microscope. In: *Principles and Techniques of Electron Microscopy VII* (Hayat MA, ed) Van Nostrand-Reinhold, New York, pp 1-78.

Jeanguillaume C, Colliex C (1989) Spectrum-image: the next step in EELS digital acquisition and processing. Ultramicroscopy **28**: 252-257.

Krivanek OL, Ahn CC, Keeney RB (1987) Parallel detection electron spectrometer using quadruple lenses. Ultramicroscopy **22**: 103-116.

Krivanek OL, Paterson JH, Poppa HR (1989) Performance of the Gatan PEELS on the VG HB501 STEM. In: *Proceedings of the 47th Annual Meeting of EMSA* (Bailey GW, ed) San Francisco Press, San Francisco, pp 410-411.

Krivanek OL, Mory C, Tence M, Colliex C (1991) EELS quantification near the single-atom level. Microsc Microanal Microstruct **2**: 257-267.

Krivanek OL, Gubbens AJ, Dellby N, Meyer CE (1992) design and first applications of a post-column imaging filter. Microsc Microanal Microstruct **3**: 187-199.

Krivanek OL, Mooney PE (1993) Applications of slow-scan CCD cameras in transmission electron microscopy. Ultramicroscopy **49**: 95-108.

Kundmann M, Chabert X, Truong K, Krivanek O (1990) EL/P software for Macintosh II computer, Gatan Inc, 6678 Owens Dr, Pleasanton, CA 94566, USA.

Körtje K-H (1994) Image-EELS: A synthesis of energy-loss analysis and imaging. Scanning Microscopy Supplement.

Lavergne J-L, Martin J-M, Belin M (1992) Interactive electron energy-loss elemental mapping by the "Imaging-Spectrum" method. Microsc Microanal Microstruct **3**: 517-528.

Leapman RD (1979) Energy loss spectroscopy of core excitations and quantitative analysis. Ultramicroscopy **3**: 413-421.

Leapman RD (1992) EELS quantitative analysis. In: *Transmission Electron Energy Loss Spectrometry in Materials Science, Minerals Metals Materials Society* (Ahn C, Disko M, Fultz B, eds) Pittsburgh (publ.), Chapter 3; 47-83.

Leapman RD, Swyt CR (1981) Electron energy-loss spectroscopy under conditions of plural scattering. In: *Analytical Electron microscopy* (Geiss RH, ed) San Francisco Press, San Francisco, pp. 164-172.

Leapman RD, Ornberg RL (1988) Quantitative electron energy loss spectroscopy in biology. Ultramicroscopy **24**: 251-268.

Leapman RD, Andrews SB (1992) Characterization of biological macromolecules by combined mass mapping and electron energy loss spectroscopy. J Microsc **165**: 225-238.

Leapman RD, Hunt JA (1992) Compositional imaging with electron energy loss spectroscopy. Microscopy: The Key Research Tool **22**: 39-49.

Leapman RD, Hunt JA, Buchanan RA, Andrews SB (1993) Measurement of low calcium concentrations in cryosectioned cells by parallel-EELS mapping. Ultramicroscopy **49**: 225-234.

Michel M, Gnägi H, Müller M (1992) Diamonds are a cryosectioner's best friend. J Microsc **166**: 43-56.

Nichols AW, Bovey PE (1989) A cryotransfer facility for the VG HB501 STEM. In: *Proceedings of the 47th Annual Meeting of EMSA* (Bailey GW, ed). San Francisco Press, San Francisco, pp 746-747.

O'Neill RR, Mitchell LG, Merril CR, Rasband WS (1989) Use of image analysis to quantitate changes in form of mitochondrial DNA after X-irradiation. Applied and Theoretical Electrophoresis **1**: 163-167.

Ottensmeyer FP (1984) Electron spectroscopic imaging: parallel energy filtering and microanalysis in the fixed-beam electron microscope. J Ultrastruct Res

88: 121-134.

Reichelt R, Engel A, Leapman RD (1986) Low dose electron energy loss spectroscopy by scanning transmission electron microscopy. In: *Proc. 11th Internat. Cong. Electron Microscopy, Kyoto* (Imura T, Maruse S, Suzuki T, eds), Japanese Electron Microsc. Soc. (publ.) 1, 33-34.

Schattschneider P, Jonas P (1993) Iterative reduction of gain variations in parallel electron energy loss spectrometry. Ultramicroscopy **49**: 179-188.

Shuman H (1981) Parallel recording of electron energy loss spectra. Ultramicroscopy **6**: 163-168.

Shuman H, Kruit P (1985) Quantitative data processing of parallel recorded electron energy loss spectra with low signal to background. Rev Sci Instrum **56**: 231-239.

Shuman H, Somlyo AP (1987) Electron energy loss analysis of near-trace elemental concentrations of calcium. Ultramicroscopy **21**: 23-32.

Somlyo AP, Bond M, Somlyo AV (1985) Calcium content of mitochondria and endoplasmic reticulum in liver frozen rapidly in vivo. Nature (London) **314**: 622-625.

Sun S, Shi S, Leapman RD (1993) Water distributions of hydrated biological specimens by valence electron energy loss spectroscopy. Ultramicroscopy **50**: 127-139.

Von Zglinicki T (1991) The measurement of water distribution in frozen specimens. J Microsc **161**: 149-158.

Wall JS (1979) Mass measurements with the electron microscope. Scanning Electron Microscopy **1979; II**: 291-302.

Wall JS, Hainfeld JF (1986) Mass mapping with the scanning transmission electron microscope. Ann Rev Biophys Chem **15**: 355-76.

Wang Y-Y, Ho R, Shao Z, Somlyo AP (1992) Optimization of quantitative electron energy loss spectroscopy in the low loss region: phosphorus L-edge. Ultramicroscopy **41**: 11-31.

Zaluzec NJ, Strauss MG (1989) Two-dimensional CCD arrays as parallel detectors in electron-energy-loss and X-ray wavelength-dispersive spectroscopy. Ultramicroscopy **28**: 131- 136.

Zierold K (1988) X-ray microanalysis of freeze-dried and frozen-hydrated cryosections. J Electron Microscopy Tech **9**: 65-82.

Discussion with Reviewers

T. von Zglinicki: How long would it take to obtain a water map from a frozen-hydrated cryosection with 100 nm resolution? How thick can the hydrated section be?

Authors: A dwell time per pixel of approximately 0.1 seconds has been used to obtain some preliminary water map data. A 128 x 128 pixel image from a 10 μm x 10 μm region of the specimen therefore takes about 1600 seconds to record. The acquisition time is limited by the read-out time of the photodiode array detector and by the speed of the computer. If the detector could be read out faster, then the probe current could be increased to maintain the same total electron dose and the data could be recorded in a much shorter time. In principle, the acquisition time could be as short as 100 seconds for a 10 μm x 10 μm image if the probe current were increased to 1 nA. The optimal specimen thickness for EELS determination of water distributions of frozen hydrated sections is one inelastic mean free path: at 100 keV beam energy this corresponds to approximately 200 nm. However, it is possible to obtain quantitative results from specimens with thicknesses in the range 100-300 nm. Processing the image data is more complicated than processing spectra because it is necessary to correct for shift of the spectrum from pixel to pixel. It is also necessary to perform several operations at each pixel, such as correction for the detector point spread function, extraction of the single scattering distributions, and multiple least squares fitting. We are currently refining techniques for routine analysis of such images.

T. von Zglinicki: You estimate a dose of 10^8 e/nm^2 as necessary for Ca mapping by EELS, however without specifying resolution. Around 10^7 e/nm^2 is probably the tolerable limit in frozen-dried cryosections, and this corresponds to about 0.1 μm resolution in X-ray microanalysis (for review, see von Zglinicki, in X-ray Microanalysis in Biology, ed by DC Sigee, AJ Morgan, AT Summer, A Warley, Cambridge University Press 1993). What would be the corresponding figure for EELS?

Authors: In our experience with the field-emission STEM terminal radiation damage occurs when the dose exceeds around 10^6 e/nm^2. At this dose one sees alteration in structure of the dried cryosections on a scale of around 20 or 30 nm. Above this dose no significant further deterioration in structure is observed even for doses $>10^8$ e/nm^2. For example, the EELS nitrogen map in Figure 8b was recorded at a dose of about 10^8 e/nm^2; features such as the endoplasmic reticulum membranes are still visible even though there is of course some loss of structure relative to the low dose dark-field image in Figure 8a. The effective microanalytical resolution for both EELS and x-ray microanalysis should be the same, i.e., approximately 30 nm in our system. This figure corresponds to a lateral deterioration in structure for membrane bound objects such as the endoplasmic reticulum in thin freeze-dried cryosections.

Meaningful analysis of compartments with high water content may only be possible on the scale of about 100 nm when radiation damage results in more severe collapse of the structure.

W.C. de Bruijn: Is the calcium reference spectrum from $CaCl_2$ crystals acquired under the same conditions as for the analysis of the cryosection? Are other types of bio-standards with calcium in a "biological" matrix not to be preferred, especially when such spectra can be acquired under the same conditions if present in the same ultrathin section?

Authors: The reference spectrum from the $CaCl_2$ salt was acquired under the same experimental conditions, i.e., with a collection semi-angle of ~20mrad, and an energy dispersion of 0.5 eV per channel. It is true that the core-edge shape in general depends on the chemical composition. However, in the case of calcium, the L_{23} edge is dominated by an atomic-like white line resonance and its edge shape does not vary strongly as a function of chemical bonding. In fact, we have found that an excellent fit is obtained by using the Ca L_{23} edge from $CaCl_2$ and have not found it necessary to use calcium in a biological matrix.

W.C. de Bruijn: The energy-loss spectrum from the 30 nm diameter ER cistern was obtained from a cryosection that was 100-200 nm thick. Is there any risk in superimposition of other elements in the deeper layers of this section?

Authors: The analyzed cisterns of ER were oriented with the membranes nearly perpendicular to the plane of the cryosection so that the analytical volume contained mainly ER. Nevertheless, some superimposition of cytoplasm was likely to have occurred. Still, the quantitative results for elements such as calcium that are concentrated within specific organelles that occupy most of the analytical volume should provide a reasonable estimate of the elemental concentration.